8978 *Biochemistry* **2010,** *49,* 8978–8987
DOI: 10.1021/bi101021e

BIOCHEMISTRY
including biophysical chemistry & molecular biology
Article

NMR Solution Structures of Clustered Abasic Site Lesions in DNA: Structural Differences between 3′-Staggered (−3) and 5′-Staggered (+3) Bistranded Lesions[†,‡]

Raphael D. Hazel[⊥,∥] and Carlos de los Santos*[,§]

[⊥]*Department of Physiology and Biophysics and* [§]*Department of Pharmacological Sciences, Stony Brook University, School of Medicine, Stony Brook, New York 11794-8651.* [∥]*Present address: Cardiac Research Department, St. Francis Hospital, Roslyn, NY 11576.*

Received June 25, 2010; Revised Manuscript Received September 8, 2010

ABSTRACT: Ionizing radiation produces a distinctive pattern of bistranded clustered lesions in DNA. A relatively low number of clustered lesions may be lethal to cells when compared to a larger number of single lesions. Enzyme cleavage experiments suggest that the orientation of bistranded lesions causes differential recognition and removal of these lesions. Like that of a previous study of bistranded abasic site lesion [Hazel, R. D., Tian, K., and de los Santos, C. (2008) *Biochemistry 47*, 11909−11919], the aim of this investigation was to determine the structures of two DNA duplexes each containing two synthetic apurinic/apyrimidinic (AP) residues, positioned on opposite strands and separated by two base pairs. In the first duplex, the AP residues are staggered in the 3′ orientation [−3 duplex, $(AP)_2$−3 duplex], while in the second duplex, the AP residues are staggered in the 5′ orientation [+3 duplex, $(AP)_2$+3 duplex]. NOESY spectra recorded in 100 and 10% D_2O buffer solutions allowed the assignment of the nonexchangeable and exchangeable protons, respectively, for each duplex. Cross-peak connectivity in the nonexchangeable proton spectra indicates that the duplex is a regular right-handed helix with the AP residues and orphan bases located inside the duplexes. The exchangeable proton spectra establish the formation of Watson−Crick G·C alignment for the two base pairs between the lesion sites in both duplexes. Distance-restrained molecular dynamics simulation confirmed the intrahelical orientations of the AP residues. The proximity of the AP residues across the minor groove of the −3 duplex and across the major groove in the +3 duplex is similar to their locations in the case of −1 and +1 clusters. This difference in structure may be a key factor in the differential recognition of bistranded AP lesions by human AP endonuclease.

Ionizing radiation produces DNA damage either by direct interaction with the DNA helix or via oxidative pathways involving the formation of free radicals (*1*−*3*). The abasic site, or apurinic/apyrimidinic (AP) lesion, is one of the many lesions produced by ionizing radiation (*1*, *2*). The mechanism for the deposition of energy by ionizing radiation is unique in its ability to produce clustered lesions, which are multiply damaged sites (MDS) within one turn of the DNA helix (*4*, *5*). Bistranded abasic clustered lesions are particularly noteworthy because their complexity poses a serious challenge to DNA repair enzymes in cells; lesions that are not repaired can be mutagenic, while misrepair can lead to apoptosis, a fact that is exploited in radiation therapy and chemotherapy for the treatment of cancer (*6*−*8*).

The orientation of clustered bistranded AP lesions affects the efficiency of DNA repair enzymes. Enzymatic studies exhibit differences in endonuclease activity depending on the arrangement of the AP lesions (*6*−*12*). When bistranded AP residues are staggered in the 3′ orientation and positioned one or three residues apart (−1 or −3 lesion), human AP endonuclease 1 (hApe1) cleaves less than 10% of either AP residue (*8*). However, when the bistranded AP residues are staggered in the 5′ orientation (+1 or +3 lesion), the enzyme exhibits significant cleavage of the AP residues, similar to that observed for a single-AP lesion duplex (*8*). Similar observations have been made with bistranded lesions located up to five nucleotides away (*9*, *10*), while those lesions located seven or more nucleotides away are processed normally with an efficiency similar to that of a single AP lesion.

The difference in DNA structure is hypothesized to be the cause of differential cleavage and repair of bistranded clustered lesions. In studies similar to ours, the structures of two pairs of DNA 13-mer duplexes containing 3′- and 5′-oriented (−1 and +1 duplexes, respectively) bistranded AP lesions have been determined (*8*, *13*). In one study, the abasic residues were separated by a G·A mismatched pair in the central sequences d(T-G-F-G)·d(A-F-A-C) and d(G-F-G-T)·d(C-A-F-A), respectively. Those results indicated that the AP residues are arranged in extrahelical bulges with the formation of a G·A mismatched pair that is coplanar in the −1 duplex, but with the G and A intercalated into the helix in the +1 duplex. In the second study, the impact on the structure and stability of a Watson−Crick G·C base pair at the center of the helix was investigated in the solution structure of a pair of related 13-mer duplexes having −1 and +1 bistranded AP clusters (*8*). In this case, the central G·C base pair adds stability to the helix at the lesion site while the AP residues are aligned with the backbone and located on either side of the minor groove in the −1 duplex or located in an extrahelical orientation on the major groove of the +1 duplex.

[†]This study was supported National Institutes of Health Grants CA77094 and CA47995.
[‡]Atom coordinates PDB accession code 2L2U; RCSB accession code RCSB101886.
*To whom correspondence should be addressed. E-mail: cds@pharm.stonybrook.edu. Telephone: (631) 444-3649. Fax: (631) 444-3218.

 Published on Web 09/09/2010

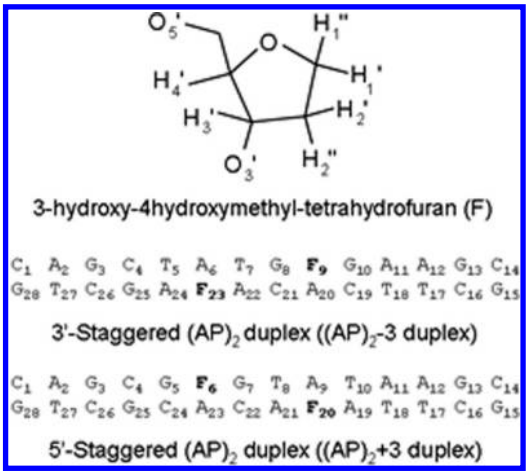

FIGURE 1: Chemical structure of a stable AP site tetrahydrofuran (THF) residue and DNA sequences of the $(AP)_2-3$ duplex and the $(AP)_2+3$ duplex. AP residues are denoted by the letter F.

The aim of this study is to further investigate the difference in DNA structure between 3′- and 5′-oriented bistranded AP clusters that are three base pairs apart. We have chosen for synthesis (*14*) a −3 duplex, designated $(AP)_2-3$ duplex, and a +3 duplex, designated $(AP)_2+3$ duplex, with bistranded THF abasic sites (Figure 1) and compare our results to those of previous studies. While the mechanism of differential recognition and cleavage inhibition of clustered AP lesions remains unresolved, the solution structures of these clustered lesions contribute to further elucidation of this phenomenon.

MATERIALS AND METHODS

Sample Preparation. AP duplexes were synthesized via the phosphoramidite chemistry method, incorporating a THF residue as previously described (*14*). Samples were purified via reverse phase HPLC and desalting using a Sephadex G-25 column, and conversion to the sodium salt was achieved with a Dowex 50W cation exchange column (*8*). Complementary strands of each duplex were annealed after using Gene Runner version 3.0 (Hasting Software Inc.) and taking UV absorption measurements at 260 Å to determine the amount of each strand that would yield a 1:1 stoichiometry. Samples were then lyophilized and dissolved in 0.7 mL of 25 mM phosphate buffer (pH 6.8) containing 50 mM NaCl and 0.5 mM EDTA in 99.96% D_2O or a 90% H_2O/10% D_2O mixture.

NMR Methods. Both one-dimensional (1D) and two-dimensional (2D) NMR spectra were recorded using a 600 MHz or 500 MHz Varian NMR spectrometer. Proton spectra were recorded for samples dissolved in 99.96% D_2O at 15 °C and in a 90% H_2O/10% D_2O mixture at 1 °C. NOESY (*15*) spectra in 100% D_2O were recorded with mixing times of 50, 100, 200, and 300 ms for distance estimates and proton assignment. COSY, DQF-COSY, and TOCSY (mixing times of 60 and 120 ms) spectra were recorded to aid in proton assignment. The repetition delay for 2D spectra collected with the sample dissolved in D_2O at 25 °C was 1.4 s, during which time a saturation pulse was applied to suppress the water signal. 1D spectra over the 5−35 °C temperature range and 2D NOESY maps (mixing times of 120 and 220 ms) at 5 °C were also recorded in 10% D_2O using a jump-return reading pulse (*16*). All 2D spectra consisted of 2048 and 300 complex data points in the t_2 and t_1 dimensions, respectively. NMR spectra were processed on a Silicon Graphics computer using Felix97 (Biosym). Before the Fourier transformation was performed, time domain data were multiplied by a sine-bell function and a convolution function, if necessary for further water suppression. NOESY, COSY, and TOCSY spectra recorded at room temperature were used to deduce the sequence specific assignment of nonexchangeable protons as previously described (*17*−*19*). The AP residues were identified via COSY spectra by their distinctive sugar protons, which appeared around a chemical shift of 4.2 ppm. The 2D spectra of exchangeable protons were used to verify the Watson−Crick alignment of internal base pairs, while the 1D spectra were used to measure the thermal stability of the duplexes.

Computational Methods. Computational modeling and restrained molecular dynamics simulations were conducted on Silicon Graphics workstations using Insight II (Accelrys, San Deigo, CA) and X-PLOR 3.1 (*20*), respectively. Structures were visualized with Midas Plus (University of California, San Francisco, Computer Graphics Laboratory), and helical parameters were computed using Curves 5.1 (*21*, *22*). Two initial models of each duplex were constructed in Insight II, starting with 14-mer A-form and B-form DNA duplexes and then replacing the purine or pyrimidine moieties with a single proton to create the THF residues. Initial models were minimized before molecular dynamics were begun.

NOE cross-peak volumes were measured from all NOESY spectra in D_2O, and interproton distances were calculated for each mixing time, using a relaxation protocol in X-PLOR. This was done for each $(AP)_2$ duplex by minimizing only the potential energy of the B-form model duplex while adjusting only the corresponding interproton distances of the model to fit the experimental peak volumes within 0.5% error bounds. One set of interproton distances was extracted from the model for each mixing time, and then the four sets of distances were averaged to produce a single set of interproton distance restraints for each $(AP)_2$ duplex. A 20% correction was applied to all experimental distances to account for the underestimation of those distances that are fixed by covalent geometry, such as cytosine H5−H6 and sugar H2′−H2″ cross-peaks. A total of 533 NOE restraints for the $(AP)_2-3$ duplex and 554 NOE restraints for the $(AP)_2+3$ duplex were derived and used for restrained molecular dynamics simulations.

The starting models of each $(AP)_2$ duplex were then refined by running restrained molecular dynamics simulations, which were conducted in vacuum using the CHARM all atom force field (*23*). Distance bounds of ±0.35 and ±0.8 Å, for distances derived from nonoverlapped and overlapped peaks, respectively, were enforced using a square well potential energy function. Watson−Crick alignments deduced from NOESY spectra in H_2O were enforced by distance restraints with bounds of ±0.1 Å, using distances derived from X-ray crystallography. Backbone and sugar pucker restraints were implemented as previously described (*8*, *17*). The four terminal residues of each duplex were restrained in the C2′-endo conformational range following the analysis of COSY45 spectra (*8*, *24*, *25*). The SHAKE algorithm was used to maintain the length of covalent bonds involving protons (*26*). Partial atomic charges on the phosphates were not reduced, leaving deoxynucleotide residues with a net charge of −1.

The simulation protocol consisted of increasing the temperature of the structures from one of four initial starting values (150, 200, 250, and 300 K) to a high temperature of 500 K in 70 ps. The scale of the NOE distance restraints was gradually increased as the temperature was increased. Simulation continued at 500 K

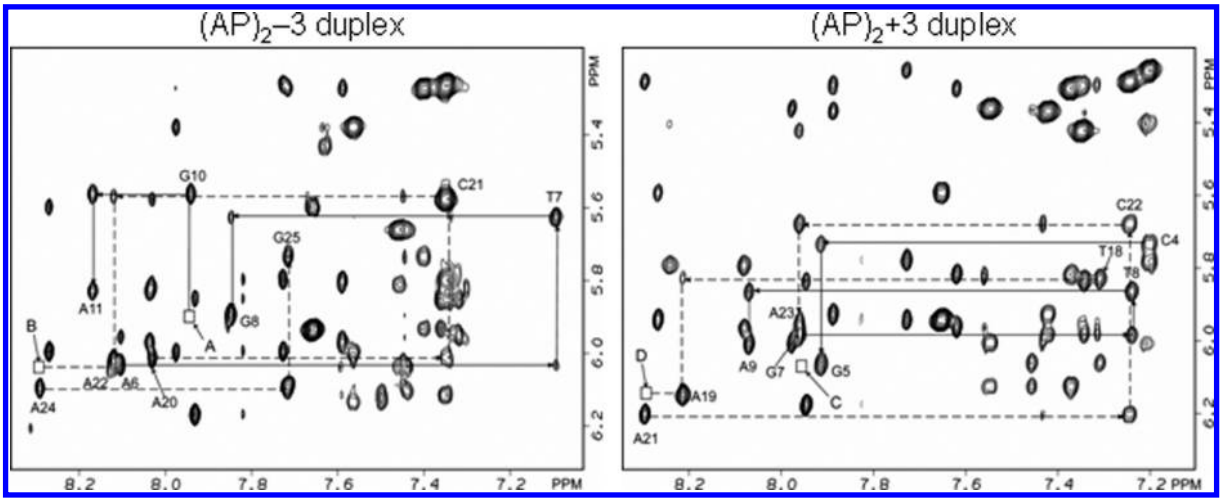

FIGURE 2: Expanded contour plot of the phase sensitive NOESY spectrum (mixing time of 300 ms) in D_2O buffer containing 50 mM NaCl, 10 mM phosphate, and 1 mM EDTA (pH 6.8) at 25 °C. Sequential connectivity in the base (7.0−8.4 ppm) and the H1′ sugar protons (5.2−6.4 ppm) is plotted for the $(AP)_2$−3 and $(AP)_2$+3 duplexes. There is no connectivity across the lesion site between residues G8 and G10 (cross-peak A missing), and in the complementary strand between A22 and A24, cross-peak B is missing for the $(AP)_2$−3 duplex. This is consistent with the intrahelical arrangement of both AP residues in the $(AP)_2$−3 duplex. In the case of the $(AP)_2$+3 duplex, no connectivity exists between residues G5 and G7 (cross-peak C missing), and in the complementary strand between residues A19 and A21, cross-peak D is missing. This is consistent with both of the AP residues being inside the helix.

for 42, 44, 46, 48, and 50 ps for five separate simulations, after which the system temperature was reduced to 300 K in 40 ps. The 20 resulting structures were put through 120 ps of restrained molecular dynamics at 300 K. Each structure was then subjected to 1000 steps of energy minimization to produce a distance-refined structure. Five final structures were chosen from the 20 structures for each $(AP)_2$ duplex. These final structures showed no NOE violations greater than 0.1 Å and exhibited pairwise root-mean-square deviation (rmsd) measurements of ≤1.2 Å. The low van der Waals energy for the refined structures was achieved by lowering the penalty NOE function during the final 120 ps of restrained dynamics at room temperature.

RESULTS

Nonexchangeable Protons. (*i*) *$(AP)_2$−3 Duplex*. The expanded NOESY contour map (mixing time of 300 ms) showing connectivity between the base (7.0−8.5 ppm) and the sugar H1′ (5.2−6.4 ppm) protons at the lesion site of the $(AP)_2$−3 duplex is plotted in Figure 2. The complete walk around the expanded NOESY plot of this same region is illustrated in Figure S1 of the Supporting Information. Cross-peak connectivity between base (pyrimidine H6/purine H8) protons and their own and 5′ flanking sugar H1′ protons indicates that the helix is right-handed in the $(AP)_2$−3 duplex. No inter-residue cross-peaks were observed between the base and the sugar H1′ protons across the lesion site, indicating no through-space connectivity between the residues separated by the AP sites. The missing cross-peaks between G8 and G10 and between A22 and A24 are indicated by arrows A and B in Figure 2, respectively, and are consistent with the arrangement of both AP residues inside the helix.

Cross-peaks between base H6/H8 protons and their own and 5′ flanking sugar H2′/2″ protons provide further evidence of the right handedness of the helix (Figure 3) for the $(AP)_2$−3 duplex. There are no cross-peaks connecting residues across the lesion sites, indicating that no connectivity through space exists between residues flanking the AP sites. Intraresidue cross-peaks are observed between H3′ protons and H2′/2″ protons of both F9 and F23, indicated by labels O, P, and P′ in Figure 3. Cross-peaks consistent with intrahelical AP residues are observed between residues G10 and F9 and between A24 and F23. These peaks were between G10(H8) and F9(H2′/2″), labeled as peak E in Figure 3, and on the complementary strand, two cross-peaks existed between A24(H8) and F23(H2″) and between A24(H8) and F23(H2′), labeled peaks B and B′ in Figure 3, respectively.

In the symmetrical base region of the NOESY spectrum, no cross-peak was observed between the residues flanking the AP sites, which is again consistent with the AP residues being inside the helix. Also supporting the intrahelical arrangement of AP residues is the existence of inter-residue cross-peaks between the AP site (H3′, H4′, and H1′/1″) protons and the 3′-flanking base protons (Figure S3 of the Supporting Information). The sugar H1′/1″ protons of the AP residues F9 and F23 are visible in COSY spectra but cannot be stereospecifically assigned. These cross-peaks occur around a chemical shift of 4.1−4.2 ppm. Cross-peaks between A24(H8) and F23(H3′), F23(H4′), and F23(H1′/1″) are labeled peaks A−C, respectively, in Figure S3 of the Supporting Information, and on the complementary strand, cross-peaks between G10(H8) and F9(H3′), F9(H4′), and F9(H1′/1″) are labeled peaks D−F, respectively, in Figure S3 of the Supporting Information.

The orphan purine bases A6 and A20 show sequential connectivity with both 5′- and 3′-flanking residues in the NOESY spectra. The sequential connectivity involving base and sugar H1′ protons through A6 in the segment (T5-A6-T7)·(A22-F23-A24) and through A20 in the segment (G8-F9-G10)·(C19-A20-C21) shown in Figure 2 and Figure S1 of the Supporting Information indicates that the orphan adenosine residues are located inside the helix at 15 °C. Sequential connectivity through these segments can also be traced in the base (7.0−8.4 ppm) and sugar H2′/2″ (3.0−1.8 ppm) region of the NOESY spectrum. In Figure 3, peaks labeled G/G′, H/H′, I/I′, and J/J′ show sequential connectivity through A6 while peaks labeled K/K′, L/L′, M/M′, and N/N′ show sequential connectivity through A20. These peaks are consistent with the arrangement of the adenosine residues inside the helix in the $(AP)_2$−3 duplex. Table S1 of the Supporting Information shows the chemical shifts of protons from each residue measured from the 2D NOESY maps of the $(AP)_2$−3 duplex.

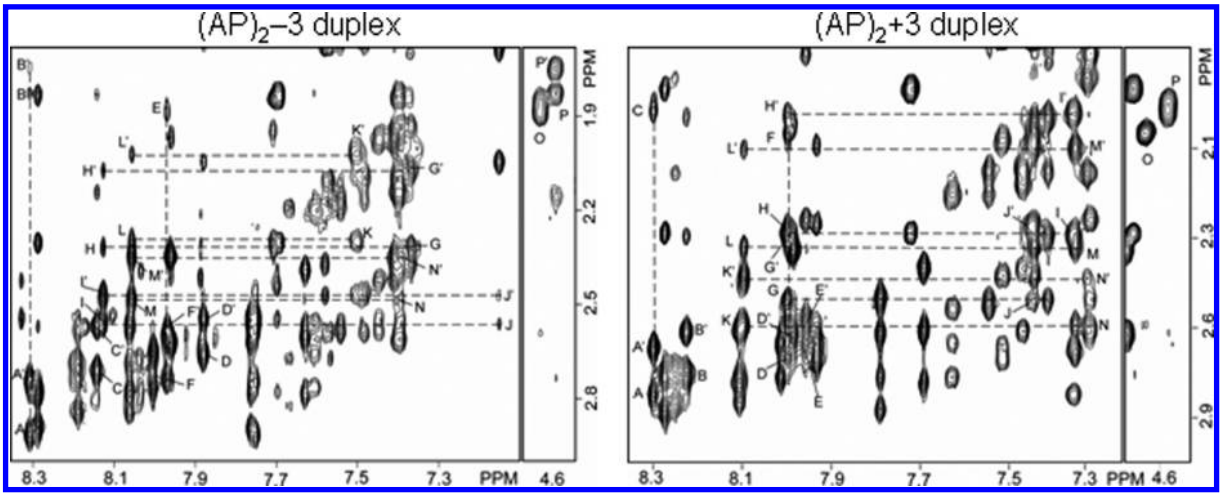

FIGURE 3: Contour plot of expanded phase sensitive NOESY spectra (mixing time of 260 ms) recorded in D_2O buffer containing 50 mM NaCl, 10 mM phosphate, and 1 mM EDTA (pH 6.8) at 25 °C. Cross-peak connectivity between base protons (7.0−8.4 ppm) and sugar H2′/2″ protons (3.0−1.8 ppm) is plotted for the $(AP)_2$−3 and $(AP)_2$+3 duplexes. Peaks in the $(AP)_2$−3 duplex are discussed in the text and are assigned as follows: A/A′, A24(H8)-A24(H2″)/A24(H2′); B/B′, A24(H8)-F23(H2″)/F23(H2′); C/C′, A22(H8)-A22(H2′)/A22(H2″); D/D′, G8(H8)-G8(H2′)/G8-(H2″); E, G10(H6)-F9(H2″/H2′); F/F′, G10(H8)-G10(H2″)/G10(H2′); G/G′, T5(H6)-T5(H2″)/T5(H2′); H/H′, A6(H8)-T5(H2″)/T5(H2′); I/I′, A6(H8)-A6(H2″)/A6(H2′); J/J′, T7(H8)-A6(H2″)/A6(H2′); K/K′, C19(H6)-C19(H2″)/C19(H2′); L/L′, A20(H8)-C19(H2″)C19(H2′); M/M′, A20(H8)-A20(H2″)/A20(H2′); N/N′, C21(H6)-A20(H2″)/A20(H2′); O, F9(H3′)-F9(H2′/2″); P/P′, F23(H3′)-F23(H2′)/F23(H2″). These peaks together confirm that both AP residues of the $(AP)_2$−3 duplex are inside the helix at the lesion site. Peaks in the $(AP)_2$+3 duplex are discussed in the text and are assigned as follows: A/A′, A21(H8)-A21(H2″)/A18(H2′); B/B′, A19(H8)-A19(H2″)/A19(H2′); C, A21(H8)-F20(H2′/2″); D/D′, G7(H8)-G7(H2″)/G7(H2′); E/E′, G5(H8)-G5(H2″)/G5(H2′); F, G7(H8)-F6(H2′/2″); G/G′, A23(H8)-A23(H2″)/A23(H2′); H/H′, A23(H8)-C22(H2″)/C22(H2′); I/I′, C22(H6)-C22(H2″)/C22(H2′); J/J′, C24(H6)-A23(H2″)/A23(H2′); K/K′, A9(H8)-A9(H2″)/A9(H2′); L/L′, A9(H8)-T8(H2″)/T8(H2′); M/M′, T8(H6)-T8(H2″)/T8(H2′); N/N′, T10(H6)-A9(H2″)/A9(H2′); O, F6(H3′)-F6(H2′/2″); P, F20(H3′)-F20(H2′/2″). The presence of these cross-peaks indicates that the AP residues in the $(AP)_2$+3 duplex are also inside the helix at the lesion site.

(*ii*) *$(AP)_2$+3 Duplex*. The expanded NOESY contour map (mixing time of 300 ms) showing through-space connectivity between the base (7.0−8.5 ppm) and the sugar H1′ (5.2−6.4 ppm) protons at the lesion site of the $(AP)_2$+3 duplex is plotted in Figure 2. The complete walk around the expanded NOESY plot of this same region is illustrated in Figure S2 of the Supporting Information. Cross-peak connectivity between base (pyrimidine H6/purine H8) protons and their own and 5′-flanking sugar H1′ protons indicates that the helix is right-handed in the $(AP)_2$+3 duplex. Again, similar to the $(AP)_2$−3 duplex, no inter-residue cross-peaks are observed between the base and the sugar H1′ protons of residues flanking the AP sites. The missing cross-peaks between G5 and G7 and between A19 and A21 are indicated by arrows C and D in Figure 2, respectively, and are consistent with the arrangement of both AP residues inside the helix in the $(AP)_2$+3 duplex.

Similar to the $(AP)_2$−3 duplex, cross-peaks between base H6/H8 protons and their own and 5′-flanking sugar H2′/2″ protons provide evidence of the right handedness of the helix (Figure 3) for the $(AP)_2$+3 duplex. Cross-peaks are absent across the lesion site, further indicating that no connectivity through space exists between residues separated by the AP sites. A cross-peak is observed between G7 and F6. This peak was assigned between G7(H8) and F6(H2′/2″) and labeled peak F in Figure 3. On the complementary strand, a cross-peak is visible between A21 and F20. This peak is assigned to A21(H8) and F20(H2′/2″) and labeled C in Figure 3. These cross-peaks are all consistent with the intrahelical arrangement of both AP residues in the $(AP)_2$−3 duplex. No cross-peak is visible between the residues flanking the AP sites in the symmetrical base region of the NOESY spectrum of the $(AP)_2$+3 duplex. The sugar H3′, H4′, and H1′/1″ protons of the AP residues display inter-residue cross-peaks with their 3′ neighboring base H8 protons. These peaks are between G7(H8) and F6(H3′), F6(H4′), and F6(H1′1″), labeled A−C, respectively, in Figure S4 of the Supporting Information, and between A21(H8) and F20(H3′), F20(H4′), and F20(H1′/1″), labeled C−E, respectively, in Figure S4. These peaks indicate that both F6 and F20 are located inside the helix. This is similar to the case for the $(AP)_2$−3 duplex, in which both AP residues exhibit similar peaks.

The orphan purine bases A9 and A23 show sequential connectivity with both 5′- and 3′-flanking residues in the NOESY spectra. The sequential connectivity involving base and sugar H1′ protons through A9 in the segment (T8-A9-T10)·(A19-F20-A21) and through A23 in the segment (G5-F6-G7)·(C22-A23-C24) as shown in Figure 2 and Figure S2 of the Supporting Information indicates that the orphan adenosine residues are located inside the helix at 15 °C. Sequential connectivity through these segments can also be traced in the base (7.0−8.4 ppm) and sugar H2′/2″ (3.0−1.8 ppm) region of the NOESY spectrum. In Figure 3, peaks labeled M/M′, L/L′, K/K′, and N/N′ show sequential connectivity through A9 while peaks labeled I/I′, H/H′, G/G′, and J/J′ show sequential connectivity through A23. These peaks are consistent with the adenosine residues being arranged inside the helix in the $(AP)_2$+3 duplex. Table S2 of the Supporting Information lists the chemical shifts of protons from each residue measured from the 2D NOESY maps of the $(AP)_2$+3 duplex.

Exchangeable Protons. (*i*) *$(AP)_2$−3 Duplex*. At low temperatures, the 1D spectrum of the $(AP)_2$−3 duplex exhibits eight partially and fully resolved spectral lines between 12.0 and 14.0 ppm that are assigned with the aid of 2D NOESY spectra (mixing time of 220 ms). From the 1D spectrum, three partially resolved signals between 13.0 and 14.0 ppm are assigned to the four thymidine imino protons while the five spectral lines between 12.0 and 13.0 ppm are assigned to five fully resolved signals of guanosine imino protons, thereby accounting for the internal Watson−Crick base pairs in the $(AP)_2$−3 duplex (Figure 4, top, and Figure 6). Signals from the terminal imino protons of G15 and G28 are not resolved at 5 °C as a result of fraying of the termini of the helix.

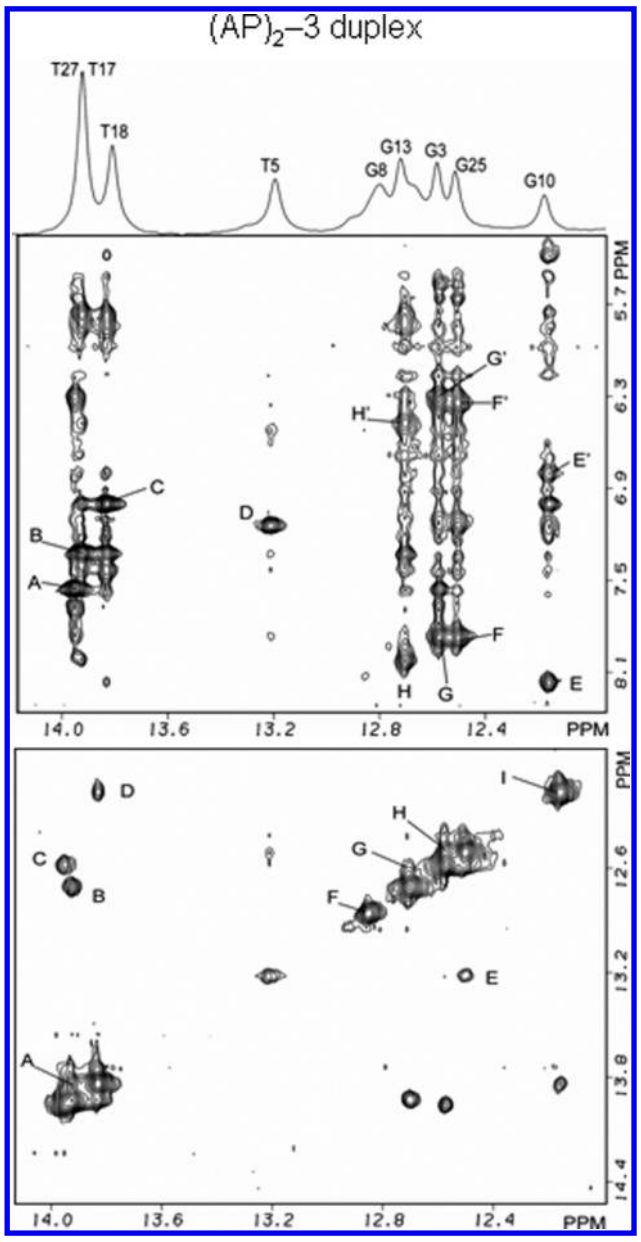

FIGURE 4: $(AP)_2-3$ duplex. Expanded phase sensitive NOESY (mixing time of 220 ms) contour plot for the $(AP)_2-3$ duplex in H_2O buffer containing 50 mM NaCl, 10 mM phosphate, and 1.0 mM EDTA (pH 6.8) at 5 °C. Cross-peaks establishing connectivity between imino protons (12.0−14.0 ppm) and the base and amino protons (8.4−5.0 ppm) have been plotted. Peaks in the $(AP)_2-3$ duplex are discussed in the text and are assigned as follows: A, T27(N3H)-A2(H2); B, T17(N3H)-A12(H2); C, T18(N3H)-A11(H2); D, T5(N3H)-A24(H2); E/E′, G10(N1H)-C19(N4Hhb)/C19(N4Hex); F/F′, G25(N1H)-C4(N4Hhb)/C4(N4Hex); G/G′, G3(N1H)-C26-(N4Hhb)/C26(N4Hex); H/H′, G13(N1H)-C16(N4Hhb)/C16(N4Hex). Cross-peak connectivity between imino protons in the symmetrical (12.0−14.0 ppm) spectral range is discussed in the text. Cross-peaks at the lesion site show the existence of Watson−Crick hydrogen bonds and regular base stacking throughout the $(AP)_2-3$ duplex. Cross-peaks in the $(AP)_2-3$ duplex are assigned as follows: A, T17(N3H)-T18(N3H); B, T17(N3H)-G13(N1H); C, T27(N3H)-G3(N1H); D, T8(N3H)-G10(N1H); E, G25(N1H)-T5(N3H); F, G8(N1H); G, G13(N1H)-G15(N1H); H, G3(N1H)-G25(N1H); I, G10(N1H).

Imino proton signals from T7 and G8 in the central segment (T7-G8)·(A22-C21) are conspicuously absent from the NOESY spectrum (Figure 4), possibly because of rapid exchange with protons of the solvent.

The phase sensitive NOESY spectrum (mixing time of 220 ms) of exchangeable protons in the $(AP)_2-3$ duplex aided in the assignment of imino and amino protons of hydrogen-bonded (hb) and exposed (ex) protons of the A·T and G·C base pairs. Two regions of interest are plotted for the expanded NOESY spectrum in Figure 4, where cross-peaks represent through-space connectivity between the imino protons of thymidine and guanosine, and cytidine amino and adenosine H2 protons, and in Figure 4, where cross-peaks represent through-space connectivity between imino protons on adjacent base pairs. In the $(AP)_2-3$ duplex, base pairs flanking the lesion site are identified through their interaction with 3′ and 5′ neighboring bases in the symmetrical spectral region of the expanded NOESY spectrum (Figure 4). For one of these flanking bases, the imino proton of T5 produces a cross-peak with the G25 imino proton near 13.2 ppm, cross-peak E in Figure 4, and is assigned to G25(H1N) and T5(N3H). The interaction between the T5 imino group and the H2 proton of A24 is fully resolved and assigned to signal D in Figure 4. At the other end of the AP segment, the imino protons of G10 and T18 produce a cross-peak at 13.9 ppm, cross peak D in Figure 4, which was assigned to G10(N1H) and T18(N3H). The imino proton of the central base T7 is not resolved; however, the imino proton signal from central base G8 produces a cross-peak in the symmetrical region of the NOESY spectrum at 12.8 ppm, peak F in Figure 4, which is assigned to G8(N1H). Watson−Crick base pair alignment is implied by the cross-peak connectivities for the remaining canonical bases throughout the duplex, and these cross-peaks are assigned in Figure 4. Additional interactions between imino protons of adjacent bases for the $(AP)_2-3$ duplex are also assigned in Figure 4.

(*ii*) *$(AP)_2+3$ Duplex*. At low temperatures, the 1D spectrum of the $(AP)_2+3$ duplex exhibits eight partially or fully resolved spectral lines between 12.0 and 14.0 ppm (Figure 5, top, and Figure 6). From the 1D spectrum of the $(AP)_2+3$ duplex, one partially resolved and two fully resolved spectral lines between 13.2 and 14.0 ppm are assigned to four thymidine imino proton signals while the five spectral lines between 12.0 and 13.2 ppm are assigned to three fully and two partially resolved signals of guanosine imino protons, thereby accounting for Watson−Crick base pairs in the $(AP)_2+3$ duplex (Figure 5, top, and Figure 6). Signals from the terminal imino protons of G15 and G28 are partially resolved at 5 °C in contrast to those in the $(AP)_2-3$ duplex, where they are not resolved.

As before, the phase sensitive NOESY spectrum (mixing time of 220 ms) of exchangeable protons in the $(AP)_2+3$ duplex aids in the assignment of imino and amino protons of hydrogen-bonded (hb) and exposed (ex) protons of the A·T and G·C base pairs. Two regions of interest are plotted for the expanded NOESY spectrum in Figure 5, where cross-peaks represent through-space connectivity between the imino protons of guanosine and thymidine, and cytidine amino and adenosine H2 protons, and in Figure 5, where cross-peaks represent through-space connectivity between imino protons on adjacent base pairs. In the $(AP)_2+3$ duplex, base pairs flanking the lesion site are identified through their interaction with 3′ and 5′ neighboring bases in the symmetrical spectral region of the expanded NOESY spectrum (Figure 4). For one of these flanking bases, the imino proton of G5 produces a cross-peak with the G25 imino proton near 12.6 ppm, cross-peak F in Figure 5, and is assigned to G5(H1N) and G5(N1H). The interactions between G5 imino and C24 amino protons are fully resolved and assigned to signals F and F′ in Figure 5. At the other end of the AP segment, the imino protons of T10 and T18 produce a cross-peak near 13.9 ppm, cross-peak

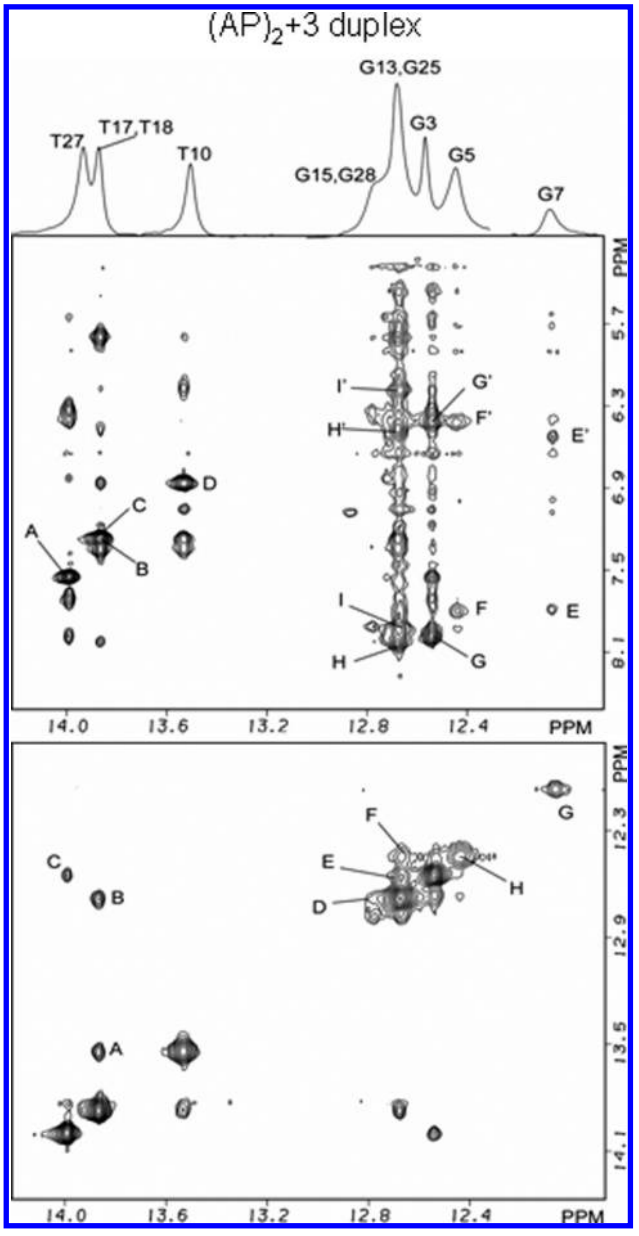

FIGURE 5: $(AP)_2$+3 duplex. Expanded phase sensitive NOESY (mixing time of 220 ms) contour plots for the $(AP)_2$+3 duplex in H_2O buffer containing 50 mM NaCl, 10 mM phosphate, and 1.0 mM EDTA (pH 6.8) at 5 °C. Cross-peaks establishing connectivity between imino protons (12.0−14.0 ppm) and the base and amino protons (8.4−5.0 ppm) have been plotted. Peaks are discussed in the text and are assigned as follows: A, T27(N3H)-A2(H2); B, T18(N3H)-A11(H2); C, T17-(N3H)-A12(H2); D, T10(N3H)-A19(H2); E/E′, G7(N1H)-C22-(N4Hhb)/C22(N4Hex); F/F′, G5(N1H)-C24(N4Hhb)/C24(N4Hex); G/G′, G3(N1H)-C26(N4Hhb)/C26(N4Hex); H/H′, G13(N1H)-C16(N4Hhb)/C16(N4Hex); I/I′, G25(N1H)-C4(N4Hhb)/C4(N4Hex). Cross-peak connectivity between imino protons in the symmetrical (12.0−14.0 ppm) spectral range is discussed in the text. Cross-peaks at the lesion site show the existence of Watson−Crick hydrogen bonds and regular base stacking throughout the $(AP)_2$+3 duplex. Cross peaks in the$(AP)_2$+3 duplex are assigned as follows: A, T18(N3H)-T10(N3H); B, T17(N3H)-G13(N1H); C, T27(N3H)-G3(N1H); D, G15(N1H)-G13(N1H); E, G25(N1H)-G3(N1H); F, G5(N1H)-G25(N1H); G, G7(N1H); H, G5(N1H).

A in Figure 5, which is assigned to T10(N3H) and T18(N3H). For the T10·A19 base pair, the imino proton of T10 and the H2 proton of A19 produce a strong signal that is assigned to cross-peak D in Figure 5. The imino proton of the central base T8 is not resolved; however, the imino proton signal from central base G7

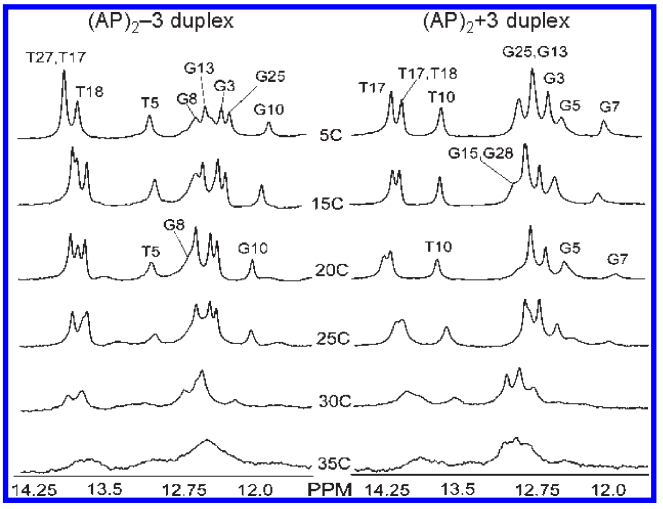

FIGURE 6: Temperature dependence of the expanded 1D NMR spectra of imino protons (12.0−14.0 ppm) of the $(AP)_2$−3 duplex (left) and $(AP)_2$+3 duplex (right) in 50 mM NaCl, 10 mM phosphate, and 1 mM EDTA as the temperature is increased from 5 to 35 °C.

produced a cross-peak in the symmetrical region of the NOESY spectrum at 12.2 ppm, peak G in Figure 5, which is assigned to G7(N1H). In contrast to the $(AP)_2$−3 duplex, the central G·C base pair can be identified through weak cross-peaks between the imino proton of G7 and the hydrogen-bonded and exposed amino protons of C22, peak E/E′ in Figure 5. Watson−Crick base pair alignment is implied by the cross-peak connectivity for the remaining canonical bases in the $(AP)_2$+3 duplex, and these cross-peaks are assigned in Figure 5. Additional interactions between imino protons of adjacent and opposite canonical bases for the $(AP)_2$+3 duplex are also assigned in Figure 5.

Thermal Stability. Figure 6 shows 1D spectra recorded at 5−35 °C. Both the $(AP)_2$−3 duplex and the $(AP)_2$+3 duplex exhibit similar melting behavior. The terminal bases of the $(AP)_2$−3 duplex are not resolved even at low temperatures, but the terminal bases of the $(AP)_2$+3 duplex produce a partially resolved spectral line at 5 °C. The spectral lines corresponding to imino proton resonances of the terminal bases of the $(AP)_2$+3 duplex disappear at 20 °C because of their fast water exchange. The central guanosine and cytidine residues between the lesion sites of both duplexes form Watson−Crick pairs as shown in the analysis of 2D NOESY spectra, but with no detectable signal for the G8·C21 base pair in the $(AP)_2$−3 duplex, and only weak signals from the G7·C22 base pair in the $(AP)_2$+3 duplex. In each duplex, the central A·T base pair does not produce a resolved imino proton signal, which is indicative of fast exchange with protons from the solvent. In both duplexes, imino proton signals from flanking thymidine residues, T5 in the $(AP)_2$−3 duplex and T10 in the $(AP)_2$+3 duplex, are shifted upfield of the other thymidine signals. Similarly, the flanking guanosine imino protons, G10 in the $(AP)_2$−3 duplex and G5 in the $(AP)_2$+3 duplex, move upfield relative to the remaining guanosine imino proton signals. Both duplexes exhibit similar behavior during the transition from helix to random coil as the temperature is increased from 5 to 35 °C with the imino proton signals of flanking A·T and G·C base pairs at the lesion site disappearing at the same rate as the internal base pairs (Figure 6). In fact, at the lesion site, flanking base pairs remain intact up to a temperature of 25 °C. A further temperature increase caused the remaining imino proton resonances to broaden and disappear above 35 °C because of their rapid exchange with water.

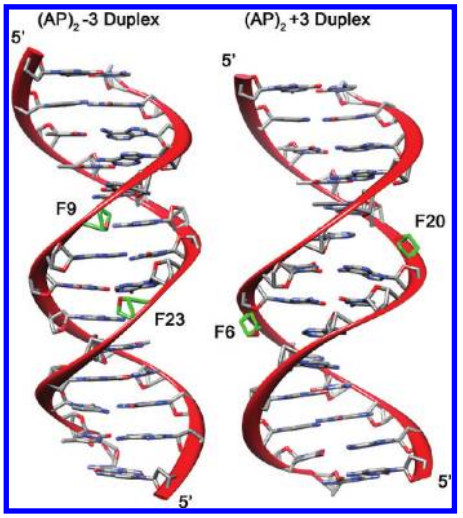

FIGURE 7: Ribbon representation of averaged minimized structures shown with the minor groove prominent. AP residues are colored green and labeled following Figure 1 numbering.

Table 1: Molecular Refinement Statistics[a]

	$(AP)_2$−3 duplex	$(AP)_2$+3 duplex
violations of covalent geometry (root-mean-square deviation)		
bond lengths (Å)	0.007	0.006
bond angles (deg)	4.04	3.81
improper angles (deg)	0.30	0.15
van der Waals (kcal/mol)	−420	−416
violations of experimental restraints (root-mean-square deviation)		
distance violations (Å) (no. of restraints)	0.012 (533)	0.007 (554)
dihedral angles (deg) (no. of restraints)	0.20 (228)	0.23 (228)

[a]Comparison of refined structures based on the root-mean-square deviations from experimental restraints and idealized covalent geometry.

Three-Dimensional Structure. The averaged minimized structures for the $(AP)_2$−3 duplex and the $(AP)_2$+3 duplex are shown in Figure 7, with the minor groove being prominent. Both duplexes are regular right-handed helices showing well-formed Watson−Crick alignments on all undamaged base pairs, including those between the abasic site residues. The AP residues are positioned in the minor groove of the helix, resulting in a shorter distance between them in the $(AP)_2$−3 duplex than in the $(AP)_2$+3 duplex. The width and depth of the major and minor grooves are normal for both $(AP)_2$ duplexes, including those at the clustered lesion site.

Table 1 summarizes statistics of the structural refinement, showing the excellent agreement with the experimental interproton NOE distances without major violations of the covalent geometry, and Table 2 lists relevant structural parameters measured for five representative models of each duplex. An overlapped stereoview of these models is shown in Figure 9. In both cases, the helices are regular, right-handed, and slightly shortened because of a bend in the helix in the direction of the major groove. Helix shortening, bend angle, and bend direction are reported in Table 2. For the $(AP)_2$−3 duplex, the AP residues are retained inside the helix with zero rotation, leaving the backbone without distortion, as shown in Figures 7−9 and Figure S5 of the Supporting Information. Similarly for the $(AP)_2$+3 duplex, both AP residues remain inside the helix, leaving the backbones undistorted as shown in Figures 7−9 and Figure S5 of the Supporting Information.

Table 2: Structural Parameters[a] of $(AP)_2$ Duplexes[b]

	$(AP)_2$−3 duplex	$(AP)_2$+3 duplex
helix shortening (%)	2.0 to 3.6	2.4 to 3.5
bend angle (deg)	15 to 34	26° to 33°
bend direction	major groove	major groove
T7 or G7 *X*-displacement, *Y*-displacement, inclination	−1.4 Å, 0.2 Å, 10.8°	−3.1 Å, −0.2 Å, 0.2°
A22 or C22 *X*-displacement, *Y*-displacement, inclination	−1.5 Å, 0.1 Å, 7.2°	−2.5 Å, −0.1 Å, 0.0°
G8 or T8 *X*-displacement, *Y*-displacement, inclination	−1.8 Å, 0.3 Å, 2.9°	−2.7 Å, 0.1 Å, −0.3°
C21 or A21 *X*-displacement, *Y*-displacement, inclination	−1.0 Å, −0.1 Å, −3.6°	−2.5 Å, −0.2 Å, 1.0°

Sugar Pucker

	$(AP)_2$−3 duplex	$(AP)_2$+3 duplex
T7 or G7	C2′-endo	C2′-endo
A22 or C22	C2′-endo	C2′-endo
G8 or T8	C2′-endo	C2′-endo
C21 or A21	C2′-endo	C2′-endo
F9 or F6	C1′-exo[c]	C2′-endo[d]
F23 or F20	C2′-endo	C2′-endo

[a]Structural parameters computed using Curves (*21*, *22*). [b]Average values measured from the converging refined structures. [c]Two structures appeared in the C2′-endo range. [d]One structure in the C1′-exo range. In both duplexes, the AP residues are fully intrahelical, exhibiting no rotation toward any of the duplex grooves.

Close-up stereoviews of the lesion site structures are shown in Figure 8. There is no significant local disturbance of the base pairs at the lesion site in the $(AP)_2$−3 duplex. Values for the base inclination and *X*- and *Y*-displacement of the orphan purine bases A6 and A20 at the lesion site are listed in Table 2. In the $(AP)_2$−3 duplex, both orphan bases undergo only small negative displacements and show small positive inclination such that they remain inside the helix (Figures 7−9 and Figure S5 of the Supporting Information). Furthermore, the central G·C and A·T base pairs retain their proper Watson−Crick alignment. Similarly for the $(AP)_2$+3 duplex, values for the inclination and *X*- and *Y*-displacement of residues A9 and A23 at the lesion site (listed in Table 2) are also small such that both orphan bases remain inside the helix. The central base pairs are undisturbed and remain in Watson−Crick alignment (Figures 7−9 and Figure S5 of the Supporting Information).

Sugar puckers for each duplex are also listed in Table 2. The $(AP)_2$−3 duplex shows regular sugar pucker in the C2′-endo conformation at the lesion site and throughout the helix, while the $(AP)_2$+3 duplex shows flexible sugar puckers with a variety of conformations at the lesion site and more regular conformations in the remainder of the duplex. In the $(AP)_2$−3 duplex, both AP residues and both orphan bases show sugar puckers in the C2′-endo conformation, with the exception of F9 adopting a C1′-exo conformation in two of the selected refined structures. The central bases show normal sugar pucker in the C2′-endo conformations. By contrast, in the $(AP)_2$+3 duplex, both AP residues adopt a normal C2′-endo conformation, with F6 adopting a C1′-exo conformation in only one of the four selected refined structures. The orphan bases show considerably more flexibility with the sugar pucker of A23 and that of A9 in the C1′-exo conformation in one of the selected structures. The central bases adopt a C2′-endo conformation.

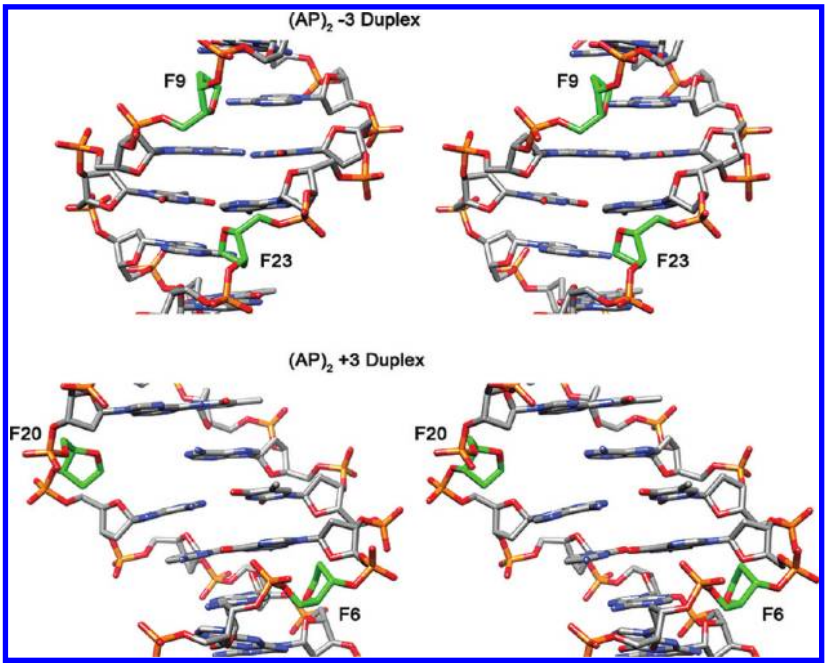

FIGURE 8: Expanded cross-eyed stereoview of the $(AP)_2-3$ cluster seen with the minor groove prominent and the $(AP)_2+3$ cluster seen with the major groove prominent, when the Watson−Crick alignments at the lesion site restraints are enforced during MD. AP residues are colored green. In the case of the $(AP)_2-3$ duplex, the AP residues are closer across the minor groove while they are farther apart across the major groove in the $(AP)_2+3$ duplex.

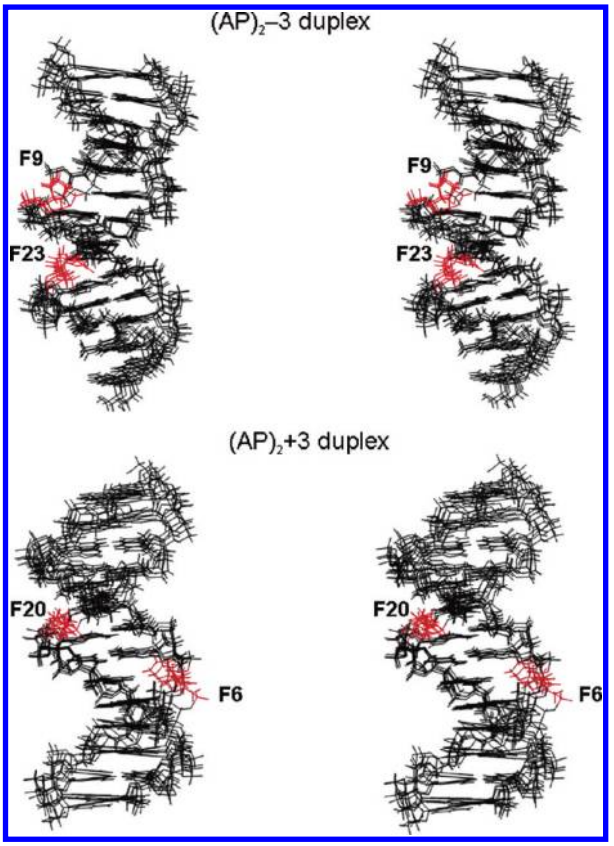

FIGURE 9: Cross-eye stereoview of five overlapped final structures shown with the minor groove prominent in the $(AP)_2-3$ duplex and the major groove prominent in the $(AP)_2+3$ duplex. AP residues are colored red.

DISCUSSION

NMR Spectra and Solution Structures of $(AP)_2$ Duplexes. The directionality of the NOE cross-peaks between base and sugar protons as well as cross-peaks present in the NOESY spectra in H_2O indicating hydrogen-bonded imino protons confirms that both helices are right-handed and stabilized by regular Watson−Crick base pair alignments (*17*−*19*). The connectivity in the fingerprint region of the NOESY spectra for both duplexes shows a continuous walk along each strand with gaps (indicated by arrows A−D in Figure 2) at the location of the AP residues, establishing that the helices are not significantly compressed at the lesion sites. Thus, residues flanking the AP sites are kept apart, while the orphan bases are stacked inside the helix. The internal stacking of orphan bases is confirmed by cross-peak connectivity with both residues flanking the orphan bases (Figures S1 and S2 of the Supporting Information). The H_2O NOESY spectra and thermal stability measurements indicate that all hydrogen bonds in both duplexes remain intact at low temperatures and melt with similar rates as the temperature increases.

Table 2 shows that, after molecular dynamics simulation, both helices are compressed by only ~3%, which is most likely due to the presence of a mild bend in the final structures. Table 2 also shows that there is similar bend in both duplexes, which may be attributed to the normal flexibility of the helix, with the tilt and inclination of the lesion site residues being negligibly small. The main difference between the duplexes emerges only after restrained molecular dynamics simulations to produce structures that are in agreement with the NMR spectra. These structures show that the AP residues are positioned differently with respect to the major and minor grooves of the helix (Figures 7−9). The refined structures, shown in stereo in Figures 8 and 9, reveal that the AP residues appear closer in space across the minor groove in the $(AP)_2-3$ duplex but are farther apart across the major groove in the $(AP)_2+3$ duplex, a situation reminiscent of previously determined structures of $(AP)_2-1$ and $(AP)_2+1$ duplexes (*8*).

Comparison of Structures and the Orientation Effect. Both AP residues on the $(AP)_2-3$ and $(AP)_2+3$ duplexes are inside the helix, a fact that differentiates them from $(AP)_2-1$ and $(AP)_2+1$ duplexes in which the AP residues sometimes form a

bulge. However, the AP residues in this study are dynamic in solution and likely to swing in and out of the helix at room temperature. Thus, these solution structures represent the average positions of the AP residues that are intrahelical in the $(AP)_2-3$ and $(AP)_2+3$ duplexes but can be extrahelical in the $(AP)_2-1$ duplex and aligned with the backbone in the $(AP)_2+1$ duplex (*8*). In studies of duplexes containing an extra adenosine, both the AP residue and the opposing adenosine were found to stack inside the helix with local perturbation of the helix extending only to the immediate flanking bases (*27*−*29*). In studies in which an opposing pyrimidine residue was inserted into the duplex, the AP residue and its counter base could be extra- or intrahelical depending on the temperature (*13*, *27*, *30*−*32*). The intrahelical character of lesion site residues in the both the $(AP)_2-3$ and $(AP)_2+3$ duplexes makes it unlikely that the differential recognition of these lesions would be based on the intrahelical position of the AP residues.

A second important feature of these structures is the fact that the AP residues are closer in space across the minor groove in the $(AP)_2-3$ duplex and farther apart in the $(AP)_2+3$ duplex. This is similar to the case for the structures of the $(AP)_2-1$ and $(AP)_2+1$ duplexes, where the AP residues are located on the minor groove in the former duplex and on opposite sides of the major groove in the latter duplex. This factor may play a role in the differential recognition of these lesions because it was found that both AP sites in the +1 and +3 orientations are cleaved by hApe1 (*8*), thus potentially producing lethal double-strand breaks. The structures of the $(AP)_2+1$ and $(AP)_2+3$ duplexes are similar and thus consistent with the observed cleavage of both AP residues. The cleavage inhibition observed in −1 and −3 clusters may relate to the fact that the AP sites are closer in space across the minor groove, hindering key interaction with the enzyme.

Three-dimensional structures of free hApe1 in solution or in a complex with AP-containing DNA have been established. hApe1 shows a barrel-like conformation in solution having a preformed active site pocket and a positively charged surface that facilitates binding to the damaged DNA (*33*, *34*). When DNA binds, the protein conformation changes very little but the enzyme induces a kink on the helical axis of the duplex and makes extensive contacts with its damaged strand at either side of the AP residue. Contacts with the unmodified strand are sparse, involving electrostatic interactions with three consecutive phosphate groups at the 5′ side of the abasic site. Because an identical set of enzyme−phosphate contacts is possible for both the $(AP)_2-3$ and $(AP)_2+3$ duplexes, or the $(AP)_2-1$ and $(AP)_2+1$ duplexes for that matter, the X-ray structure of the complex does not provide a definitive answer to the question of why differential recognition occurs (*35*). It is possible that the structural differences among clustered $(AP)_2$ duplexes are sensed during an initial recognition step, which would be sensitive to the proximity of a second AP site across the minor groove of the duplex. Alternatively, it is conceivable that the second AP site on the nonscissile strand of the duplex would increase backbone flexibility, hindering hApe1−phosphate contacts only in the case of the −1 and −3 3′-staggered clusters.

CONCLUSIONS

Through oxidative damage, ionizing radiation produces clustered DNA damage, of which clustered abasic sites are quite prevalent. They can be mutagenic if not repaired or become a source of potentially lethal double-strand breaks during the repair process. Abortive repair of bistranded AP clusters is particularly prone to the production of double-strand breaks, a phenomenon that is exploited in radiation therapy and chemotherapy. However, the orientation of bistranded lesions factors significantly in the efficiency with which they are removed from DNA, a fact attributed to differential recognition of these lesions by the repair machinery. We have determined the structures of $(AP)_2-3$ and $(AP)_2+3$ bistranded duplexes and shown that they are similar to the previously determined structures of the $(AP)_2-1$ and $(AP)_2+1$ duplexes in that the AP residues are located close in space across the minor groove in the $(AP)_2-3$ and $(AP)_2-1$ duplexes but are farther apart in the $(AP)_2+3$ and $(AP)_2+1$ duplexes. The structures of $(AP)_2$ duplexes show the common factor of closeness in space of the AP residues that are not cleaved by the hApe1 enzyme. Factors such as the thermodynamic stability of the damaged duplexes or the position the AP residues in an extrahelical bulge do not correlate with the differential recognition of these DNA lesions. The fact that hApe1 (or bacterial exo-III) readily processes +1 and +3 $(AP)_2$ bistranded lesions while cleavage of −1 and −3 clusters proceeds at very slow rates would suggest that the repair of clustered AP lesions has evolved to fundamentally avoid the presence of DSB with 3′-protruding ends.

ACKNOWLEDGMENT

We thank Mr. Erich Bremer for providing computer support services and help in the creation of figures and Ms. Cecilia Torres for the synthesis and purification of modified oligodeoxynucleotides. Molecular graphics images were produced using the MidasPlus program from the Computer Graphics Laboratory, University of California, San Francisco (supported by National Institutes of Health Grant RR-01081).

SUPPORTING INFORMATION AVAILABLE

Proton chemical shifts of the $(AP)_2-3$ and $(AP)_2+3$ duplexes (Tables S1 and S2), contour plots of NOESY spectra (mixing time of 300 ms) depicting base-H1′ proton connectivities for the $(AP)_2-3$ and $(AP)_2+3$ duplexes (Figures S1 and S2), contour plots of the same NOESY spectra showing interactions among protons of the furan residues in the $(AP)_2-3$ and $(AP)_2+3$ duplexes (Figures S3 and S4), and space filling representations of the $(AP)_2-3$ and $(AP)_2+3$ duplex structures (Figure S5). This material is available free of charge via the Internet at http://pubs.acs.org.

REFERENCES

1. Ward, J. F. (1998) DNA Damage Produced by Ionizing Radiation in Mammalian Cells: Identities, Mechanisms of Formation and Reparability. *Prog. Nucleic Acids Res. Mol. Biol. 35*, 95–125.
2. Halliwell, B., and Aruoma, O. I. (1991) DNA damage by oxygen derived species: Its mechanism and measurement in mammalian systems. *FEBS Lett. 281*, 9–19.
3. Newcomb, T. G., and Loeb, L. A. (2001) Oxidative Damage and Mutagenesis. In DNA Damage and Repair. Volume 1: DNA Repair in Higher Eukaryotes, Humana Press Inc., Totowa, NJ.
4. Sutherland, B. M., Bennett, P. V., Sidorkina, O., and Lavall, J. (2000) Clustered Damages and Total Lesions Induced in DNA by Ionizing Radiation: Oxidized Bases and Strand Breaks. *Biochemistry 39*, 8026–8031.
5. Sutherland, B. M., Bennett, P. V., Sidorkina, O., and Lavall, J. (2000) Clustered damages induced in isolated DNA and human cells by low doses of ionizing radiation. *Proc. Natl. Acad. Sci. U.S.A. 97*, 103–108.
6. Weinfeld, M., Rasouli-Nia, A., Chaudhury, M. A., and Britten, R. A. (2001) Response of Base Excision Repair Enzymes to Complex DNA Lesions. *Radiat. Res. 156*, 584–589.

7. David-Cordonnier, M.-H., Cunniffe, S. M. T., Hickson, I. D., and O'Neill, P. (2002) Efficiency of Incision of an AP Site within Clustered DNA Damage by the Major Human AP Endonucleases. *Biochemistry 41*, 634–642.
8. Hazel, R. D., Tien, K., and de los Santos, C. (2008) NMR Solution Structures of Bistranded Abasic Site Lesions in DNA. *Biochemistry 47*, 11909–11919.
9. Georgakilas, A. G., Bennet, P. V., Wilson, D. M., III, and Sutherland, B. M. (2004) Processing of bistranded abasic DNA clusters in γ-irradiated human hematopoetic cells. *Nucleic Acids Res. 32*, 5609–5620.
10. Chaudhry, M. A., and Weinfeld, M. (1997) Reactivity of Human Apurinic/Apyrimidinic Endonuclease and *Escherichia coli* Exonuclease III with Bistranded Abasic Sites in DNA. *J. Biol. Chem. 272*, 15650–15655.
11. Chaudhry, M. A., and Weinfeld, M. (1995) The Action of *Escherichia coli* Endonuclease III on Multiply Damaged Sites in DNA. *J. Mol. Biol. 249*, 914–922.
12. Harrison, L., Hatahet, Z., and Wallace, S. S. (1999) In virto Repair of Synthetic Ionizing Radiation-induced Multiply Damaged DNA Sites. *J. Mol. Biol. 290*, 667–684.
13. Lin, Z., and de los Santos, C. (2001) NMR Characterization of Clustered Bistrand Abasic Site Lesions: Effect of Orientation on their Solution Structure. *J. Mol. Biol. 308*, 341–352.
14. Takeshita, M., Chang, C.-N., Johnson, F., Will, S., and Grollman, A. P. (1987) Oligodeoxynucleotides Containing Synthetic Abasic Sites: Model substrates for DNA polymerases and apurinic/apyrimidinic endonucleases. *J. Biol. Chem. 262*, 10171–10179.
15. States, D. J., Haberkorn, R. A., and Ruben, D. J. (1982) A two-dimensional nuclear Overhauser experiment with pure absorption phase in four quadrants. *J. Magn. Reson. 48*, 286–292.
16. Plateau, P., and Gueron, M. (1982) Exchangeable proton NMR without baseline distortion, using new strong-pulse sequences. *J. Am. Chem. Soc. 104*, 7310–7311.
17. van de Ven, F. J., and Hilbers, C. W. (1988) Nucleic acids and nuclear magnetic resonance. *Eur. J. Biochem. 178*, 1–38.
18. de los Santos, C. (1999) Probing DNA structure by NMR Spectroscopy. In Comprehensive Natural Products Chemistry. Volume 7: DNA and Aspects of Molecular Biology, Elsevier Science Ltd., Oxford, U.K.
19. Hare, D. R., Wemmer, D. E., Chou, S. H., Drobny, G., and Reid, B. (1983) Assignment of the non-exchangeable proton resonances of d(C-G-C-G-A-A-T-T-C-G-C-G) using two-dimensional nuclear magnetic resonance methods. *J. Mol. Biol. 171*, 319–336.
20. Brunger, A. (1993) X-PLOR version 3.1. A System for X-ray Crystallography and NMR, Yale University Press, New Haven, CT.
21. Lavery, R., and Sklenar, H. (1988) The definition of generalized helicoidal parameters and axis of curvature for irregular nucleic acids. *J. Biomol. Struct. Dyn. 6*, 63–91.
22. Lavery, R., and Sklenar, H. (1989) Defining the structure of irregular nucleic acids: Conventions and principles. *J. Biomol. Struct. Dyn. 6*, 655–667.
23. Brooks, B., Bruccoleri, R., Olafson, B., States, D., Swaminathan, S, and Karplus, M. (1983) CHARMM: A program for macromolecular energy, minimization, and dynamics calculations. *J. Comput. Chem. 4*, 187–217.
24. Rinkel, L. J., and Altona, C. (1987) Conformational analysis of deoxyrybofuranos ring in DNA by means of sums of proton-proton coupling constants: A graphical method. *J. Biomol. Struct. Dyn. 4*, 621–649.
25. Majumdar, A., and Hosur, R. V. (1992) Simulation of 2D NMR spectra for determination of solution conformations of nucleic acids. *Prog. NMR Spectrosc. 24*, 109–158.
26. Ryckert, J.-P., Ciccoti, G., and Berendsen, H. J. C. (1977) Numerical integration of the Cartesian equations of motion of a system with constraints-molecular-dynamics of N-alkanes. *J. Comput. Phys. 23*, 327.
27. Beger, R. D., and Bolton, P. H. (1998) Structures of Apurinic and Apyrimidinic Sites in Duplex DNAs. *J. Biol. Chem. 273*, 1565–1573.
28. Wang, K. Y., Parker, S. A., Goljer, I., and Bolton, P. H. (1997) Solution Structure of a Duplex DNA with an Abasic Site in a dA Tract. *Biochemistry 36*, 11629–11639.
29. Kalnik, M. W., Norman, D. G., Zagorski, M. G., Swann, P. F., and Patel, D. J. (1989) Conformational Transitions in Cytidine Bulge-Containing Deoxytridecanucleotide Duplexes: Extra Cytidine Equilibrates between Looped Out (Low Temperature) and Stacked (Elevated Temperature) Conformations in Solution. *Biochemistry 28*, 294–303.
30. Cuniasse, P., Sowers, L. C., Eritja, R., Kaplan, B., Goodman, M. F., Cognet, J. A., LeBert, M., Guschlbauer, W., and Fazakerley, G. V. (1987) An abasic site in DNA. Solution conformation determined by proton NMR and molecular mechanics calculations. *Nucleic Acids Res. 15*, 8003–8022.
31. Kalnik, M. W., Chang, C.-N., Johnson, F., Grollman, A. P., and Patel, D. J. (1989) NMR Studies of Abasic Sites in DNA Duplexes: Deoxyadenosine Stacks into the Helix Opposite Acyclic Lesions. *Biochemistry 28*, 3373–3383.
32. Kalnik, M. W., Chang, C.-N., Grollman, A. P., and Patel, D. J. (1988) NMR Studies of Abasic Sites in DNA Duplexes: Deoxyadenosine Stacks into the Helix Opposite Cyclic Analogue of 2-Deoxyribose. *Biochemistry 27*, 924–931.
33. Gorman, M. A., Morera, S., Rothwell, D. G., de La Fortelle, E., Mol, C. D., Tainer, J. A., Hickson, I. D., and Freemont, P. S. (1997) The crystal structure of the human DNA repair endonuclease HAPE1 suggests the recognition of extra-helical deoxyribose at DNA abasic sites. *EMBO J. 16*, 6548–6558.
34. Beernink, P. T., Segelke, B. W., Hadi, M. Z., Erzberger, J. P., Wilson, D. M., III, and Rupp, B. (2001) Two Divalent Metal Ions in the Active Site of a New Crystal Form of Human Purinic/Apyrimidinic Endonuclease, Ape1: Implications for the Catalytic Mechanism. *J. Mol. Biol. 307*, 1023–1034.
35. Clifford, D., Mol, C. D., Izumi, T., Mitra, S., and Tainer, J. A. (2000) DNA-bound structures and mutants reveal abasic DNA binding by APE1 DNA repair and coordination. *Nature 403*, 451–456.